AIAA AVIATION Forum
5-9 June 2017, Denver, Colorado
23rd AIAA/CEAS Aeroacoustics Conference

Level-educed Wavepacket Representation of Mach 1.8 Laboratory-Scale Jet Noise

Tracianne B. Neilsen,[1] Aaron B. Vaughn,[2] Kent L. Gee,[3]
Brigham Young University, Provo, UT, 84602

Masahito Akamine,[4] Koji Okamoto,[5]
Graduate School of Frontier Sciences, University of Tokyo, Kashiwa, Chiba, 277-8561, Japan

Susumu Teramoto,[6]
Graduate School of Engineering, University of Tokyo, Bunkyo-ku, Tokyo, 113-8656, Japan

Seiji Tsutsumi[7]
Japan Aerospace Exploration Agency, Sagamihara, Kanagawa, 252-5210, Japan

The search for an equivalent acoustic source model for high-speed jet noise has recently focused on wavepacket representations. A wavepacket is defined as a spatially extended source with an axial amplitude distribution that grows, saturates and decays, an axial phase relationship that produces directional noise, and correlation lengths longer than the integral length scales of the turbulent structures. This definition of a wavepacket has the same characteristics as the large-scale turbulent mixing noise; if the turbulent mixing noise can be isolated, the associate equivalent acoustic wavepacket—defined as a pressure fluctuation on a cylinder around the jet nozzle—can be found. An estimate of the frequency-dependent, spatial variation in the large-scale turbulent mixing noise comes from a similarity spectra decomposition of the measured autospectral density, which in turn leads to data-educed wavenumber axial spectra associated with the frequency-dependent equivalent wavepackets. This wavepacket eduction technique has been applied to acoustical measurements of an unheated, Mach 1.8 jet in the near and far fields. At both locations, the resulting frequency-dependent, data-educed wavenumber spectra exhibit different types of self-similarity for low and high frequency regimes that become apparent when the axial wavenumber is scaled by the acoustic wavenumber, with a transition band between the two regimes. As expected, the data-educed wavenumber spectra can be used to predict field levels in the dominant radiation lobe. Addition of an uncorrelated source distribution, derived from the similarity spectra decomposition associated with the fine-scale turbulent mixing noise, creates a model that accounts for the sideline levels. This field-prediction ability of the wavepacket-plus-uncorrelated-distribution model is tested using the near and far field measurements. When predicting the field at the other location, the model's average error is less than 2 dB for St = 0.04-0.25 but increases for larger St because the apparent directivity changes from near to far field, likely due to the frequency dependence of the extended source region.

[1] Part-Time Assistant Professor, Dept. of Physics and Astronomy, N283 ESC, AIAA Member.
[2] Undergraduate Student, Dept. of Physics and Astronomy, N283 ESC.
[3] Associate Professor, Dept. of Physics and Astronomy, N283 ESC, AIAA Senior Member.
[4] Ph.D. Candidate, Dept. of Advanced Energy, Graduate School of Frontier Sciences, AIAA Member.
[5] Associate Professor, Dept. of Advanced Energy, Graduate School of Frontier Sciences, AIAA Member.
[6] Associate Professor, Dept. of Aeronautics and Astronautics, Graduate School of Engineering, AIAA Senior Member.
[7] Associate Senior Researcher, Aerospace Research and Development Directorate, Research Unit III, AIAA Member.

Nomenclature

a_n = stochastic random function
A = normalization factor
c = ambient sound speed
D_j = jet nozzle diameter
f = frequency
G_n = axial wavenumber spectrum
$|G_0|$ = scaled, frequency-dependent, data-educed axial wavenumber spectrum
$\boldsymbol{k}$ = wavenumber vector
k = acoustic wavenumber
k_z = axial wavenumber
k_r = radial wavenumber
$L_{w,\mathrm{far}}$ = far-field levels due to a wavepacket
L_{far} = far-field levels due to a wavepacket + uncorrelated source distribution
M_c = convective Mach number
n = azimuthal mode number
OASPL= overall sound pressure level
p = acoustic pressure
p_{ref} = reference pressure
p_w = pressure modeled by a wavepacket
r_0 = radius of the nozzle
r = radius in cylindrical coordinates
R = radius in spherical coordinates
S = spatially dependent autospectral density
$S_{w,\mathrm{far}}$ = modulus of the square pressure due to a wavepacket
$S_{u,\mathrm{far}}$ = modulus of the square pressure for an uncorrelated source distribution
St = Strouhal number
t = time
U_c = convective velocity
U_j = jet velocity
z = axial distance
ϵ = frequency-dependent amplitude
ϕ = azimuthal angle
θ = polar angle
λ = wavelength
ρ_j = jet density
ω = angular frequency

I. Introduction

Wavepacket representations of jet noise strive to provide a model consistent with linear stability theory of the mean flow[1,2] that incorporates features of the highly directional turbulent mixing noise.[3,4,5] A wavepacket has been described as a spatially extended source characterized by an axial amplitude distribution that grows, saturates and decays, an axial phase relationship that produces directional noise,[6] and correlation lengths longer than the integral length scales of the turbulence.[7] Wavepacket characteristics are found in the turbulent region, the hydrodynamic near field and the acoustic far field.[3] However, depending on the convective Mach number (relative to the ambient sound speed), a wavepacket describes either primarily convectively subsonic sound radiation or the highly directional Mach wave radiation (convectively supersonic). The goal is to create a wavepacket model of jet noise that can be employed in future noise environment modeling and noise reduction efforts.

Based on linear stability theory,[1,2] techniques have been proposed to use far-field measurements to infer wavepackets that model the radiating portion of the pressure fluctuations.[8] Morris[9] and Papamoschou[10,11] present two methods for obtaining wavepacket representations with the same goal: for a single frequency, connect far-field

measured spectral levels with a wavepacket representation of the source radiated pressure projected on a near-field cylinder centered on the jet centerline. Morris[9] showed how the spatial distribution of levels from the large-scale similarity spectrum decomposition of far-field spectra yield frequency-dependent, axial wavenumber spectra for a range of jet velocities. Papamoschou proposed an analytical wavepacket model to predict far-field sound levels. Because both methods begin with far-field noise, information is not available about the nonradiating, evanescent components of the turbulent pressure variations in the hydrodynamic near field. Nevertheless, the acoustic field contains information sufficient to obtain an equivalent wavepacket model representative of the levels of the propagating noise. These two methods were combined in Neilsen et al.[12] to obtain the first wavepacket-based representation of the directional component of noise from a high-performance military aircraft.

Several additional questions regarding the data-educed axial wavenumber spectra are investigated using noise from a jet facility at the Hypersonic High-enthalpy Wind Tunnel at Kashiwa Campus of the University of Tokyo. The unheated, Mach 1.8 jet was ideally expanded through a 20-mm diameter converging-diverging nozzle. After a background section that summarizes the wavenumber spectrum eduction technique and the method for predicting the field levels, both are applied to the autospectral densities along a line array a $10D_j$ from the jet centerline and a arc with a $40D_j$ radius. The impact of distance on the data-educed wavenumber spectra are investigated and self-similar regimes are shown. Preliminary investigations into using the data-educed wavenumber spectra for field predictions do not account for the sideline sound radiation. A method is proposed for obtaining a frequency-dependent uncorrelated source distribution from the fine-scale similarity spectrum decompositions. The combination of the wavepacket and the uncorrelated source distribution is used as an equivalent source model to predict the sound field.

II. Background

In this paper, two methodologies are linked together and expanded to create a frequency-dependent wavepacket model for noise near a Mach 1.8 laboratory-scale jet. First, the measured spectra are decomposed into the two similarity spectra for turbulent mixing noise given by Tam *et al.*[15] Following the derivations in Refs. 13, 14, and 9, the spatial dependence of levels associated with the large-scale similarity spectrum provides estimates of the axial wavenumber spectrum of the wavepacket as a function of frequency. These wavenumber spectra can be used to obtain estimates of the far-field noise levels associated with large-scale turbulent mixing noise.[10] Because this single wavepacket model underestimate sound levels outside the dominant radiation lobe, an uncorrelated source distribution based on the fine-scale similarity spectral components is included. The theoretical foundations for eduction of the wavenumber spectra and subsequent field predictions are presented in this section. The nomenclature has been modified slightly from the original presentations to provide a consistent framework tying the methods together. A more detailed derivation is found in Ref. 12.

A. Level-educed Wavenumber Spectra

One model for jet noise postulates that sound radiated from the jet exhaust plume is generated by turbulent mixing noise from fine-scale and large-scale turbulent structures. Tam *et al.*[15] used an extensive database of laboratory-scale jet data and found an empirical similarity spectrum associated with each kind of turbulent mixing noise. To the sideline, the fine-scale similarity (FSS) spectrum matches the radiated noise spectrum for a range of jet operating conditions. Similarly, the large-scale similarity (LSS) spectrum approximates the directional radiation associated with the large-scale turbulent mixing noise, often referred to as the Mach cone. In between these two regions, a combination of the FSS and LSS spectra is needed to account for the spectral shape. Examples of the decomposition of measured jet noise spectra into FSS and LSS spectral components are found in Morris,[9] Tam *et al.*,[4,15-17] and Viswanathan,[18-20] for laboratory-scale jets and for military aircraft engines in Schlinker *et al.*[21] and Neilsen *et al.*[22-23] When this spectral decomposition is performed for an array of microphones, the spatial variation in the levels associated with the LSS spectral component at frequency f can be tied to the axial wavenumber spectrum of an equivalent acoustic wavepacket.

The connection between the axial wavenumber spectrum and the spatially dependent autospectral density associated with the LSS spectral decomposition, S, begins with the solution to the wave equation for pressure fluctuations, p, from a wavepacket represented as a normalized eigenfunction expansion. The three-dimensional wave equation in cylindrical coordinates (r, z, ϕ) is

$$\frac{\partial^2 p}{\partial t^2} - c^2\left(\frac{\partial^2 p}{\partial r^2} + \frac{1}{r}\frac{\partial p}{\partial r} + \frac{1}{r^2}\frac{\partial^2 p}{\partial \phi^2} + \frac{\partial^2 p}{\partial z^2}\right) = 0.$$

The general solution, $p(r, \phi, z, t)$, can be represented in terms of its Fourier transforms with respect to time, t, and axial distance, z, as well as a Fourier series in the azimuthal angle, ϕ:

$$p(r, \phi, z, t) = \frac{1}{(2\pi)^3}\sum_{n=-\infty}^{n=\infty}\int_{-\infty}^{\infty}\int_{-\infty}^{\infty} P_n(r, k_z, \omega)e^{i(n\phi + kz - \omega t)}d\omega dk_z, \tag{1}$$

with ω as the angular frequency and k_z as the axial wavenumber. From the wave equation, the corresponding ordinary differential equation for $P_n(r, k_z, \omega)$ is

$$\frac{d^2 P_n}{dr^2} + \frac{1}{r}\frac{dP_n}{dr} + \left(\omega^2 - k_z^2 - \frac{n^2}{r^2}\right)P_n = 0. \tag{2}$$

The solution to the radial portion of Eq. (2) are the Hankel function of the first kind of order n: $H_n^{(1)}(k_r r)$, with k_r as the radial wavenumber. Because $P_n(r_0, k_z, \omega)$ is the radially dependent, wavenumber/frequency spectrum of the pressure fluctuations of the n^{th} azimuthal mode on a cylindrical surface of radius r_0, a normalization factor of $H_n^{(1)}(k_r r_0)$ is included. A modal series expansion for $P_n(r, k_z, \omega)$—the Fourier transform (according to Eq. (1)) of the acoustic pressure on a cylinder a radial distance r from the jet centerline—is written as

$$P_n(r, k_z, \omega) = \frac{a_n(\omega)H_n^{(1)}(k_r r)}{H_n^{(1)}(k_r r_o)}G_n(k_z, \omega), \tag{3}$$

where $a_n(\omega)$ is a stochastic random function of frequency. (The relationship between k_r, k_z, and k, the acoustic wavenumber, is $k^2 = k_r^2 + k_z^2$.) The normalized axial eigenfunctions, $G_n(k_z, \omega)$, are the frequency-dependent, axial wavenumber spectra.

Subsequent steps in the derivation yield an expression for the autospectral density, S, in terms of $G_n(k_z, \omega)$. Inverse Fourier transforms with respect to ω and k_z of Eq. (3) yields an expression for the pressure fluctuations at $r \geq r_o$:

$$p(r, \phi, z, t) = \frac{1}{(2\pi)^3}\sum_{n=-\infty}^{n=\infty}\int_{-\infty}^{\infty}\int_{-\infty}^{\infty}\frac{a_n(\omega)H_n^{(1)}(k_r r)}{H_n^{(1)}(k_r r_o)}G_n(k_z, \omega)e^{i(n\phi + kz - \omega t)}d\omega dk_z. \tag{4}$$

The Fourier transform with respect to time of the autocorrelation of $p(r, \phi, z, t)$ is the spatially dependent autospectral density:

$$S(r, z, \omega) = \frac{A^2}{2\pi}\rho_j^2 U_j^3 D_j \sum_{n=-\infty}^{\infty}\left|\int_{-\infty}^{\infty} G_n(k_z, \omega)\frac{H_n^{(1)}(k_r r)}{H_n^{(1)}(k_r r_o)}e^{ik_z z}dk_z.\right|^2, \tag{5}$$

where D_j is the diameter of the jet nozzle, ρ_j and U_j are the density and speed of the jet, and A is a normalization factor. Thus, $S(r, z, \omega)$ can be expressed as the sum over azimuthal modes of the inverse Fourier transform with respect to k_z of $G_n(k_z, \omega)$.

Use of only the $n = 0$ term in Eq. (5) can often provide a good approximation, especially for lower frequency noise from axisymmetric jets.[9,14,16] Restriction to only the $n = 0$ term is also applicable if the measurements span a limited azimuthal aperture so as to lack sufficient information to estimate the contributions from higher-order azimuthal modes ($n > 0$). In this case, an azimuthally averaged result is obtained. Thus, the relationship between

the measured autospectral density, S and the scaled magnitude of $G_0(k_z,\omega)$, the axial eigenfunction of order zero, is revealed by using $n = 0$ in Eq. (5).

Several steps are needed to show how to obtain $G_0(k_z,\omega)$ from measured $S(r,z,\omega)$. First, a transformation is made from cylindrical to spherical coordinates using $z = R\cos(\theta)$ and $r = R\sin(\theta)$, where R is the distance from the origin to the point at (r,z), and θ is the angle relative to the z axis. Next the Hankel function of the first kind is replaced by its asymptotic form for large arguments: $H_0^{(1)}(\zeta) \to \sqrt{\frac{2}{\pi\zeta}}e^{i\left(\zeta-\frac{\pi}{4}\right)}$. Then the integral in Eq. (5) is evaluated by the method of stationary phase to obtain s

$$S(R,\theta,\omega) = \frac{A^2}{2\pi}\rho_j^2 U_j^3 D_j \left|\frac{2}{R}\frac{G_0(k_z,\omega)}{H_0^{(1)}(k_r r_o)}\right|^2.$$

This expression can be rewritten as

$$\frac{A^2|G_0(k_z,\omega)|^2}{D_j^2} = \frac{\pi}{2\rho_j^2 U_j^3}\left(\frac{R}{D_j}\right)^2 \left|H_0^{(1)}(k_r r_0)\right|^2 \frac{S(R,\theta,\omega)}{D_j} s \tag{6}$$

Equation (6) relates the data-educed estimates of the axial Fourier transforms of frequency-dependent wavepackets associated with the $n = 0$ azimuthal mode on a cylindrical surface, of radius r_0 concentric with the nozzle exit, to the measured autospectral density in $S(R,\theta,\omega)$. The square-root of the left-hand side of Eq. (6) is referred to as the scaled, frequency-dependent, data-educed axial wavenumber spectrum, $|G_0(k_z,\omega)|$. Examples of $|G_0(k_z,\omega)|$ for the unheated, Mach 1.8 jet are shown in Sec. IVA.

B. Far-field levels

Both Morris[9] and Papmoschou[10] describe how the axial wavenumber spectrum, $G_n(k_z,\omega)$, of a wavepacket can be used to model far-field sound pressure levels generated by the n^{th} azimuthal mode. For a single angular frequency, ω, the integral in Eq. (4) can be divided into two parts corresponding with subsonic and supersonic wavenumbers:

$$p_{w,\text{sub}}(n,r,\phi,z,t) = \frac{1}{2\pi}e^{-i\omega t+in\phi}\int_{|k_z|>\omega/c_0} G_n(k_z)\frac{H_n^{(1)}(k_r r)}{H_n^{(1)}(k_r r_0)}e^{ik_z z}dk_z$$

$$p_{w,\text{sup}}(n,r,\phi,z,t) = \frac{1}{2\pi}e^{-i\omega t+in\phi}\int_{-\omega/c_0}^{\omega/c_0} G_n(k_z)\frac{H_n^{(1)}(k_r r)}{H_n^{(1)}(k_r r_0)}e^{ik_z z}dk_z\ . \tag{7}$$

With the asymptotic form of $H_n^{(1)}(k_r r)$ for large arguments, Eq. (7) yields an expression for the pressure at far-field position in spherical coordinates due to the supersonic portions of the equivalent wavepacket's pressure fluctuations that propagate to the far field:

$$p_{w,\text{far}}(n,R,\theta,\phi,t) = -\frac{i\epsilon}{\pi R}\left(\frac{G_n(k_z)}{H_n^{(1)}(k_r r_0)}\right)e^{ikR}e^{-i\omega t+in\phi}, \tag{8}$$

where R is the distance from the origin, θ is the angle from the wavepacket (jet) axis z, ϕ is the azimuthal angle, and ϵ is a frequency-dependent scaling factor. The modulus of the squared pressure at angular frequency ω is the autospectral densities from the equivalent wavepacket:

$$S_{w,\text{far}}(n,R,\theta,\phi) = \left(\frac{\epsilon}{\pi R}\right)^2 \left|\frac{G_n(k_z)}{H_n^{(1)}(k_r r_0)}\right|^2. \tag{9}$$

The associated levels, in decibels, predicted at this far-field location due to the n^{th} order wavepacket is

$$L_{w,\text{far}}(n,R,\theta,\phi) = 10\log\left(\frac{\left|S_{w,\text{far}}(n,R,\theta,\phi)\right|^2}{p_{\text{ref}}^2}\right), \tag{10}$$

where p_{ref} = 20 μPa/$\sqrt{\text{Hz}}$. These predicted levels can be compared to measured levels to evaluate the validity of this level-based wavepacket model for the large-scale turbulent mixing noise.

The far-field levels generated from a single wavepacket, as in Eq.(10), do not adequately predict the spatial radiation pattern of jet noise. $L_{w,\text{far}}$ captures the directional radiation associated with the large-scale turbulent mixing noise but not the sound levels outside of the dominant radiation lobe. Papamoschou [10] found it necessary to add a monopole to capture the levels of the jet noise to the sideline of the nozzle exit (large polar angles). A different approach is taken in this paper: A second uncorrelated source distribution is included to account for the sideline levels. The wavenumber spectrum for this uncorrelated distribution is obtained from the spatially dependent autospectral levels obtained from the FSS spectral decomposition, and an equation similar to Eq. (6) is used to obtain levels modeled by the uncorrelated source distribution, $S_{u,\text{far}}$. Combination of this FSS spectrum-based field component with the far-field pressure from the LSS spectrum-based wavepacket, $S_{w,\text{far}}$ from Eq. (9), yields total predicted spectral levels of

$$L_{\text{far}}(n,R,\theta,\phi) = 10\log\left(\frac{\left|S_{w,\text{far}}(n,R,\theta,\phi)\right|^2 + \left|S_{u,\text{far}}(n,R,\theta,\phi)\right|^2}{p_{\text{ref}}^2}\right), \tag{11}$$

where the subscripts w and u indicated wavepacket model and uncorrelated source distribution, respectively. The ability of the wavepacket plus uncorrelated distribution to predict measured spectral levels is investigated in Sec. IVB.

III. Measurements

A. Experiment Description

The performance of the data-educed wavenumber spectra and field prediction algorithms is tested on acoustical measurements in a jet facility at the Hypersonic High-enthalpy Wind Tunnel at Kashiwa Campus of the University of Tokyo. The unheated jet was ideally expanded through a 20-mm diameter converging-diverging nozzle for a design Mach number of 1.8.[25] Although the facility is not anechoic, nearby reflecting surfaces were wrapped in fiberglass to limit reflections. Favorable matches to anechoic measurements by Greska[24] were shown previously by Akamine *et al*.[25]

Data from two microphone arrays are shown in this paper: a far-field arc and a near-field line array (shown in Figure 1). The stationary, 16-channel polar microphone arc contained G.R.A.S. 40BE, Type 1, prepolarized microphones, which spanned θ = 15°-90°, relative to the jet exhaust centerline, with 5° resolution. The arc microphones were located at a radial distance of 40 nozzle diameters (D_j), and the arc was centered about the measurement array reference points (MARP) at $10D_j$ downstream from the jet exit. The near-field line array consisted of 16 G.R.A.S. 46BG microphones, which have sensitivities less than 0.3 mV/Pa and permit peak sound pressure level measurements in excess of 180 dB. The line array microphones were arranged in a line with adjacent microphones spaced $1D_j$ apart. For all measurements, the microphone gridcaps were removed.

Calibrated acoustic pressure waveform data were acquired at a sampling rate of 204.8 kHz using National Instruments PXI-4498 cards. During each jet blow, which lasted between 60-90 seconds, data were acquired in 6.1 second intervals as the near-field microphone array was moved to several positions using a two-axis, stepper-controlled positioning system. For each test, the jet facility ambient pressure, temperature, and humidity were recorded using a Kestrel 4500B weather station. The ambient sound speed was 348 m/s during the measurements used in this study. Additional information about the measurements is found in Ref. 26.

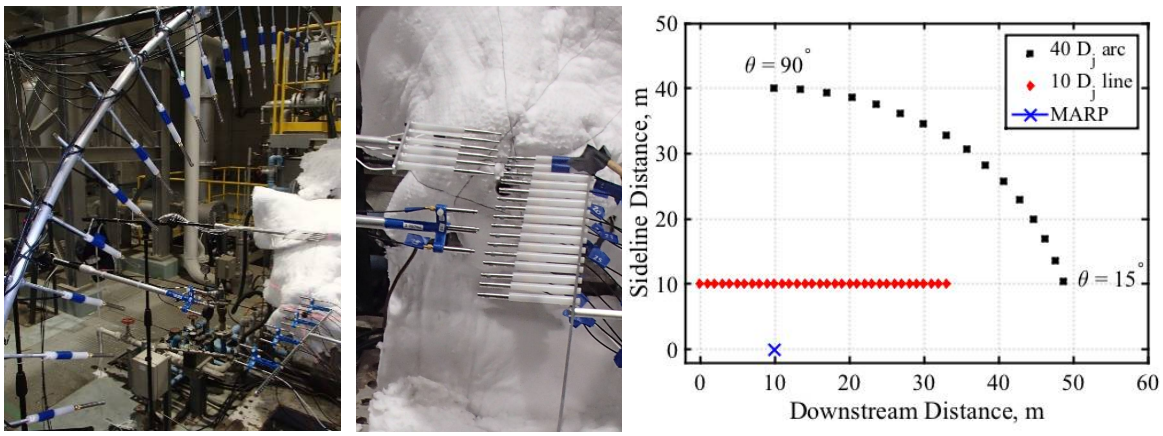

Figure 1 Photographs of the 16-channel, $40D_j$ arc (left) and the $10D_j$ line array (middle) and schematic of the experiment (right).

B. Spectral Characterization

Far-field data from a range of cold and heated supersonic laboratory-scale jets were used by Tam *et al.*[15] to develop two similarity spectra that match the primary features of the noise from the fine-scale structures and the large-scale structures. The large-scale similarity (LSS) spectrum, which has a relatively narrow peak and power-law decay on both sides, was reported to fit the data for aft angles. On the other hand, the fine-scale similarity (FSS) spectrum, with its broader peak and a more gradual roll-off at both high and low frequencies, matched the radiated spectra to the sideline direction. Tam *et al.* [15] proposed that jet noise at any radiation angle can be represented as either the LSS or FSS spectra or a combination of the two, and subsequent studies have shown this to generally be the case. For example, Tam *et al.*[27] have summarized the agreement between laboratory-scale data for Mach 0.7, 1.5 and 1.96 jets with T_{ratio}=1.8 and the similarity spectra. In addition, many studies on subsonic and supersonic, laboratory-scale jets conducted by Viswanathan have shown, in general, support for the similarity spectra.[20,18,28]

Details of the similarity spectra decompositions for the unheated, Mach 1.8 jet shown in Figure 1 are reported by Vaughn *et al*[29] and summarized here. As noted by Morris,[9] there is some leeway in defining the parameters that match the similarity spectra to measured spectral shapes. In this case, two guidelines are applied. First, the decompositions primarily strive for agreement in the peak frequency region. In addition, the contributions to the OASPL associated with the FSS and LSS spectral components are constrained to grow or decay smoothly as a function of downstream distance. Examples of similarity spectra fits at select microphones on the line array at $10D_j$ and $40D_j$ are shown in Figure 2 and Figure 3, respectively. (The relationship between downstream distance z and the angles θ are shown in the schematic in Figure 1.) The spatial regions over which the LSS or FSS spectra, or a combination of the two spectra provide the best fits are illustrated in Figure 4, in which the contributions of the LSS and FSS spectral components to the overall sound pressure level (OASPL) are compared to the measured OASPL on the $10D_j$ line array (blue) and the $40D_j$ arc (red). The similarity spectra decompositions match the measured autospectral densities and follow the expected spatial trends.

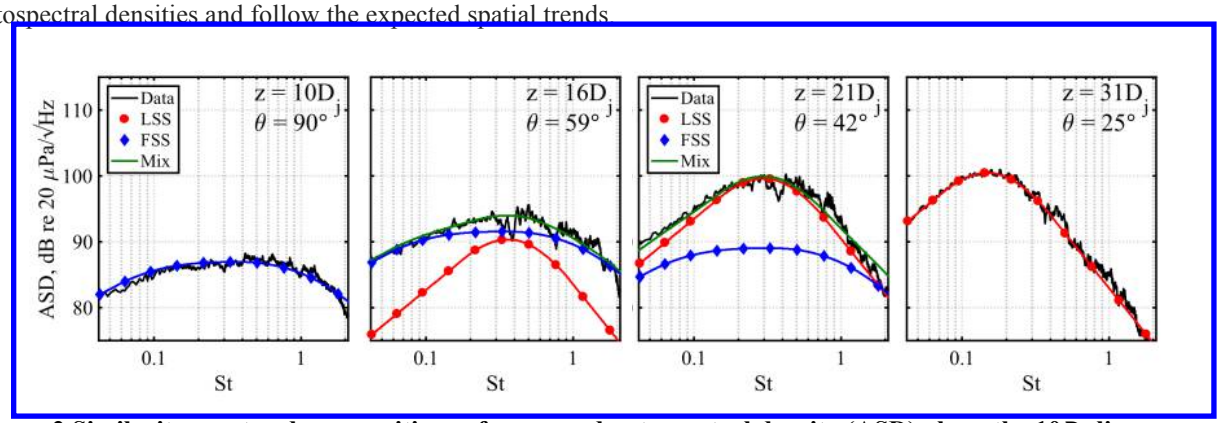

Figure 2 Similarity spectra decompositions of measured autospectral density (ASD) along the $10D_j$ line array.

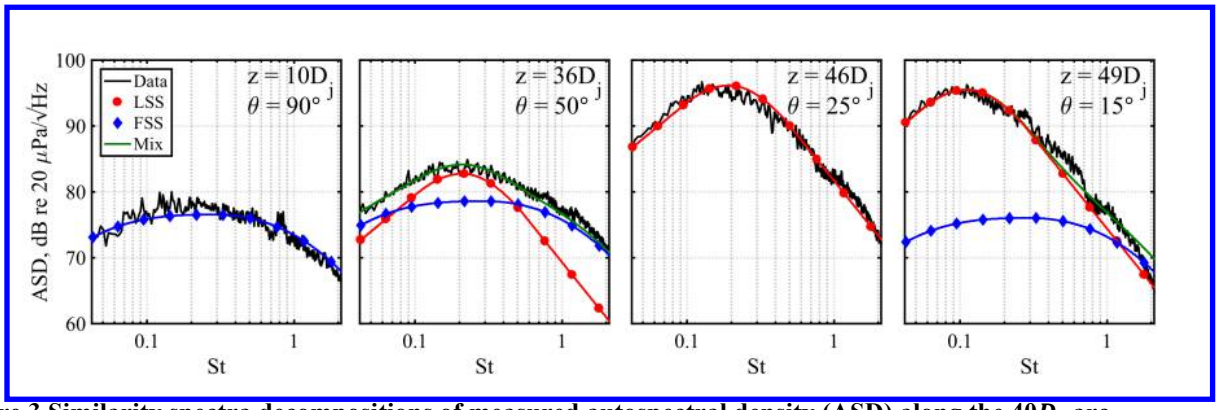

Figure 3 Similarity spectra decompositions of measured autospectral density (ASD) along the $40D_j$ arc.

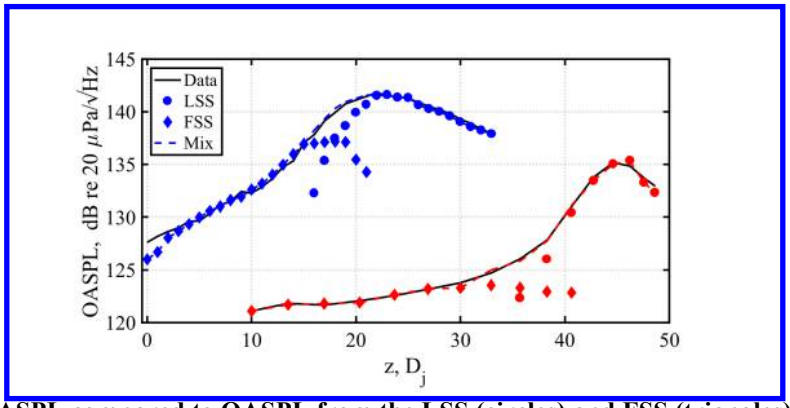

Figure 4 Measured OASPL compared to OASPL from the LSS (circles) and FSS (triangles) spectra components on the $10D_j$ line array (blue) and the $40D_j$ arc (red).

While similarity spectra decompositions are usually compared to the spectral levels at a single location (as in Figure 2Figure 3), the wavenumber spectrum eduction procedure described in Sec. IIA relies on the spatial dependence of the decomposed LSS and FSS spectral densities at a single frequency. Comparisons of the spatial dependence of the LSS and FSS spectral densities to measured autospectral density are shown in the top plots of Figure 5 for St = 0.1 and 0.2 and in Figure 6 for St = 0.4 and 0.8, which correspond to approximately 2.4, 4.8, 9.6, and 19.1 kHz. The measured autospectral densities are displayed as solid black lines, LSS spectral densities as circles, FSS spectral densities as diamonds, and the combination, when applicable, as a dashed line. The levels on the $10D_j$ array are in blue and the $40D_j$ arc in red. In general, the spatial distribution of measured and decomposed levels agree well. These similarity spectra decompositions provide the foundation for the axial wavenumber spectra eduction method as the spatial variation in LSS autospectral density is the $S(R,\theta,\omega)$ used in Eq. (6) to obtain $|G_0(k_z,\omega)|$.

IV. Results

Based on $S(R,\theta,\omega)$ from the $10D_j$ line array and the $40D_j$ arc, two sets of $|G_0(k_z,\omega)|$ are obtained. The $|G_0(k_z,\omega)|$ obtained from the two measurement arrays are compared in Sec. IVA to illustrate the difference between near and far-field applications of this method. The variations of the $|G_0(k_z,\omega)|$ with frequency are similar to those in Ref. 9. When k_z is scaled by k, however, the normalized $|G_0(k_z/k,\omega)|$ exhibit two frequency regions of self-similarity with a transition band between them, something not previously noted. The ability of the two sets of $|G_0(k_z,\omega)|$ and their accompanying FSS-based uncorrelated source distributions to predict measured autospectral densities is explored in Sec. IVB.

A. Level-Educed Wavenumber Spectra

The spatial variation in LSS autospectral density, at a single frequency, is the $S(R,\theta,\omega)$ used in Eq. (6) to estimate the the scaled axial wavenumber spectrum, $|G_0(k_z,\omega)|$. Only wavenumber components corresponding to the supersonic, propagating components $|k_z| \leq \omega/c$, are useful as they correspond to real values of θ. This statement is better understood by considering the relationship between the acoustic, axial, and radial wavenumbers. For a sound wave of angular frequency ω traveling in a medium with wave speed c, the magnitude of the acoustic wavenumber is $k = \omega/c$, and the wavenumber vector, $\boldsymbol{k}$, points in the direction the wave is traveling. In cylindrical coordinates, the angle at which the wavenumber vector points relative to the z axis is $\theta = \tan^{-1}(k_r/k_z)$, where the z and r components of the acoustic wavenumber vector are $k_z = k\sin\theta$ and $k_r = k\cos\theta$. The wavenumber associated with radial direction, $k_r = \pm\sqrt{k^2 - k_z^2}$, is real if $|k_z| \leq \omega/c$ and, in such cases, corresponds with waves propagating outward from the source. Such wavenumbers are called sonic (when equal) or supersonic, signifying trace wavenumber matching in the axial direction. Note that $k_r = \pm\sqrt{k^2 - k_z^2}$ is imaginary when $k_z > k$. The positive or negative sign associated with the square root is chosen such that when $k_z > k$ (subsonic wavenumbers), the associated wavenumber components decay evanescently with radial distance.

The data-educed axial wavenumber spectra are first displayed as a function of $k_z D_j$ to facilitate comparisons with the cases shown in of Ref. 9. The $|G_0(k_z,\omega)|$ obtained from the LSS autospectral densities on the $10D_j$ line array (blue) and $40D_j$ arc (red) are shown in the lower plots of Figure 5 for St = 0.1 and 0.2 and in Figure 6 for St = 0.4 and 0.8. At low St, $|G_0(k_z,\omega)|$ increases over the entire range of supersonic k_z values—as seen at St = 0.1 for both locations—similar to those shown for the slower jet velocities in Figure 4 of Ref. 9. The lack of a wavenumber peak in $|G_0(k_z,\omega)|$ indicates that at these frequencies, the jet conditions do not permit trace wavenumber matching, and consequently, indicates a convectively subsonic case. For higher St, the peak in the wavenumber spectra occurs at supersonic k_z, similar to the higher jet velocity cases in Figure 4 of Ref. 9. The wavenumber corresponding to the peak in $|G_0(k_z,\omega)|$, $k_{z,\mathrm{peak}}$, is directly related to the convective velocity, U_c, and directionality of the dominant radiation lobe, θ_{peak}, for that frequency: $U_c = \omega/k_{z,\mathrm{peak}}$ and $\cos\theta_{\mathrm{peak}} = k_{z,\mathrm{peak}}/k$. From the plots of $|G_0(k_z,\omega)|$, it appears that more of wavenumber spectrum is convectively supersonic as frequency increases, as shown in Figure 7(b), such that the trace wavenumber matching produces efficient sound radiation at greater angles, relative to the jet centerline, at higher frequencies.

These observations, however, need to be reconsidered because of the frequency scaling inherent in the definitions of U_c and θ_{peak}. The impact of the frequency dependence is uncovered by looking at normalized $|G_0(k_z/k,\omega)|$, as shown in Figure 7(b) at select St for the $10D_j$ array. The normalized $|G_0(k_z/k,\omega)|$ have the same shape and no evidence of a peak for St = 0.05 and 0.1, get broader and have a peak that shifts left as St increases, and then reach a different shape and peak value for St = 0.8 and 1.6. (It should be noted that the discrete values of k_z at which the $|G_0|$ are defined limit the resolution.) Further evidence for two distinct, low and high frequency, self-similar regimes is shown in Figure 8 where normalized $|G_0(k_z/k,\omega)|$ are plotted for St = 0.05-4. The transition band between the two self-similar regimes occurs over St ~ 0.17-0.6 for the $10D_j$ array case. The transition band begins lower and is narrower for the normalized $|G_0(k_z/k,\omega)|$ from the arc: St ~ 0.12-0.4. The cause of this difference in the transition band is not currently understood, The presence of these two self-similar regions is significant because much of the literature talk about the self-similarity of the large-scale turbulent mixing noise from jets, but it appears there are two distinct regimes of self-similarity with a transition band between the two. Wavepacket-based models for jet noise need to account for this difference.

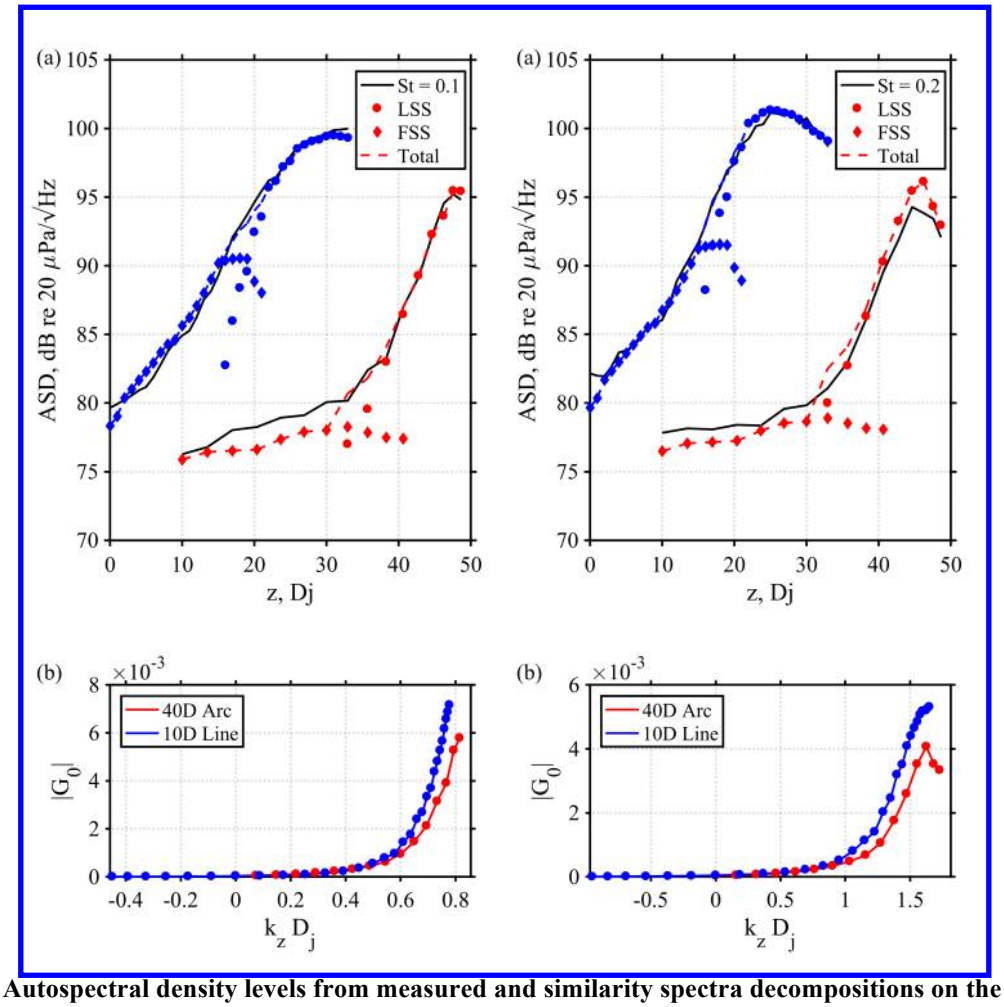

Figure 5 (a) Autospectral density levels from measured and similarity spectra decompositions on the 10D line array (blue) and 40D arc (red) at St = 0.1 (left) and St = 0.2 (right) and (b) the corresponding LSS spectra-educed axial wavenumber spectra, $|G_0|$.

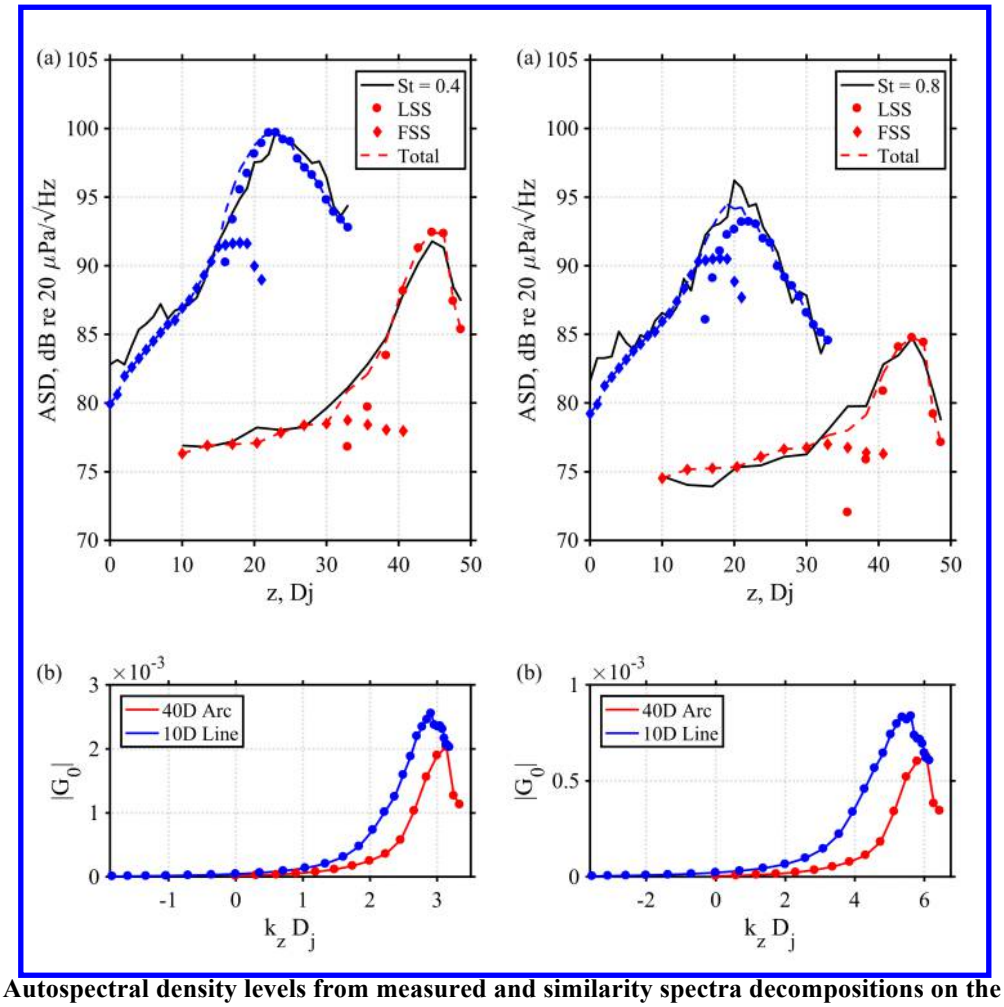

Figure 6 (a) Autospectral density levels from measured and similarity spectra decompositions on the 10D line array (blue) and 40D arc (red) at St = 0.4 (left) and St = 0.8 (right) and (b) the corresponding LSS spectra-educed axial wavenumber spectra, $|G_0|$.

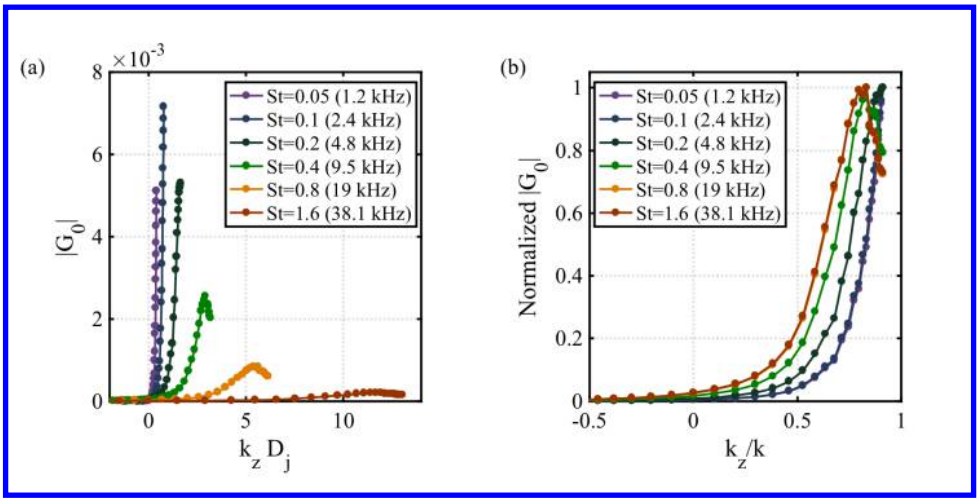

Figure 7 Data-educed, axial wavenumber spectra, $|G_0|$, from the LSS autospectral densities at the $10D_j$ line array as a function of (a) k_zD_j and (b) k_z/k after being normalized.

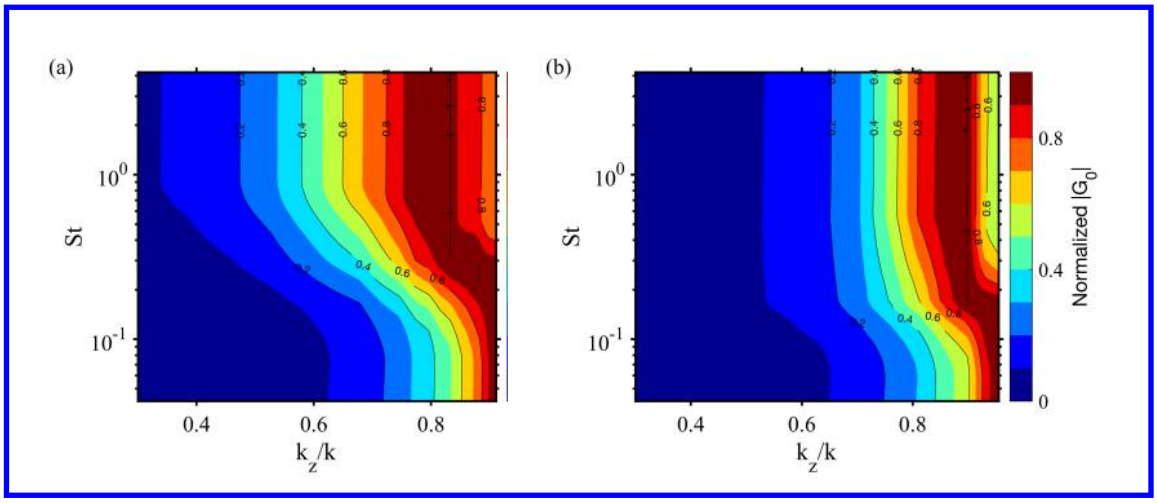

Figure 8 Frequency-dependent axial wavenumber spectra educed from LSS spectra decompositions on the line array at $10D_j$ (left) and the $40D_j$ arc (right).

When comparing the normalized $|G_0(k_z/k,\omega)|$ for the two arrays in Figure 8, it is important to note that these differences are not due to simply the change in distance. Likewise, scaling the measurements to a common far-field distance does not change these results, because, as can be seen in Eq. (4), geometric scaling of levels by distance R is removed by the calculation for $|G_0|$ in Eq. (6). Rather, the differences in the data-educed wavenumber spectra from the line array at 10 D_j (left) and the 40 D_j arc (right) are likely related to physical differences in the measured sound fields.

B. Far-field Predictions

In constructing an equivalent source representation of the turbulent mixing noise, a principle question is whether a single wavepacket is sufficient to predict the radiated field. To address this question, the autospectral density levels, $L_{w,\mathrm{far}}$—predicted from the $|G_0(k_z,\omega)|$from the LSS autospectral densities via Eq. (10)—are compared with the measured levels, as are the predicted levels that occur from the addition of an uncorrelated source distribution, as described in Eq. (11). In this work, scaling factors $\epsilon(\omega)$ in Eq. (9) are used to match the peak value of the predicted and measured levels at the starting location, i.e., the location used to generate the $|G_0(k_z,\omega)|$. These scaling factors are then used to predict the field at other locations.

The wavepacket-based predicted levels, $L_{w,\mathrm{far}}$—computed from the $|G_0(k_z,\omega)|$ in Eq. (10)—are designed to capture the strong directional radiation associated with the large-scale turbulent mixing noise. Examples of $L_{w,\mathrm{far}}$ for St = 0.4-2 as a function of downstream distance, z, in terms of D_j, are shown in Figure 9(a) for the $10D_j$ line array case (left) and the $40D_j$ arc (right) using their respective $|G_0(k_z,\omega)|$. When compared to the measured levels, L_{meas} (shown in Figure 11(a)) the $L_{w,\mathrm{far}}$ matches the spectral levels in the main radiation lobe but underestimate the levels elsewhere. Papamoschou[10] observed this behavior as well when using a single wavepacket and added a monopole to account for sideline radiation.

In this work, an alternative approach is used; an FSS spectra-based wavenumber spectra associated with an uncorrelated source distribution is obtained following a similar procedure to that described for the $|G_0(k_z,\omega)|$, which is used to predict the fine-scale turbulent mixing noise contribution to the sound field. Field predictions from the uncorrelated distributions are shown in Figure 9(b), for the $10D_j$ line array case (left) and the $40D_j$ arc (right). The total predicted field is the combination of the LSS and FSS-based predictions, L_{far} in Eq. (11). Examples are shown in Figure 9(c). L_{far} captures the measured, spatially dependent autospectral levels (L_{meas}in Figure 10(a)) much better than the LSS-based $L_{w,\mathrm{far}}$ alone.

As a benchmark, the difference between L_{far} and L_{meas} using the same input and prediction locations are shown in Figure 10(b) such that negative values indicate $L_{\mathrm{meas}} > L_{\mathrm{far}}$. At most angles and frequencies, L_{far} is within 0-2 dB of L_{meas}. The error plots in Figure 10(b) show the consistency of the method: The data-educed wavenumber spectra from an LSS spectra-based wavepacket plus an FSS spectra-based uncorrelated source distribution can

produce the levels at the starting locations. The real test of the method, however, is whether the wavenumber spectra educed from one measurement array can correctly predict the levels at a different location.

The preliminary investigations into the robustness of this data-educed wavenumber spectra method as a prediction tool show promise at low St and point to additional factors that must be considered for larger St. As an example of inward propagation, the wavenumber spectra educed from the $40\ D_j$ arc similarity spectral decompositions are used to predict the levels on the $10D_j$ line array. Extrapolation of the wavenumber spectra is required because the two measurement apertures span a different set of angles, θ (relative to the z axis and the MARP) and $k_z = k\cos\theta$. The resulting L_{far} is displayed in Figure 11(a,left). Extrapolation effects cause the results for $z < 10D_j$ to be unphysical, illustrating the difficulty of predicting portions of the sideline sound field that are not captured by the input array. The errors $L_{\text{far}} - L_{\text{meas}}$ are shown in Figure 11(b,left). For $z > 12D_j$, the prediction is reasonable as the average error magnitude is $|L_{\text{far}} - L_{\text{meas}}| < 2$ dB for St < 0.25. For higher St, however, the error is greater. Similar features are seen for the outward propagation example in the right plots in Figure 11 when the $|G_0(k_z, \omega)|$ from the $10D_j$ line array measurements are used to predict L_{far} on the $40D_j$ arc. The downstream extrapolation of wavenumber spectra ($z > 34D_j$) works better than the upstream extrapolation, likely due to the difference in the field correlations. For this outward propagation case, $|L_{\text{far}} - L_{\text{meas}}| < 2$ dB for St < 0.25 and increases at higher St, but in the opposite directions as the inward propagation case. A cause for this frequency-dependent error needs to be found.

A clue into the source of the errors for St > 0.25 can be seen by comparing $|G_0(k_z, \omega)|$ from the two measurement locations. As shown in Figure 6, the peaks in the $|G_0(k_z, \omega)|$ occur at different values of k_z, such that $k_{z,\text{peak}}$ for the near-field case ($10D_j$ line array) is less than for the far-field case ($40D_j$ arc). Because $\cos\theta_{\text{peak}} = k_{z,\text{peak}}/k$, the difference in $k_{z,\text{peak}}$ corresponds to a difference in directivity. This difference can also be seen in Figure 8. For the $40D_j$ arc, $\theta_{\text{peak}} = 32°$ compared to $\theta_{\text{peak}} = 24°$ for the $10D_j$ line array.

One possible cause for the discrepancy in θ_{peak} obtained from the $10D_j$ line array and the $40D_j$ arc relates to the frequency-dependent nature of the extended jet noise source. A study of the acoustic vector intensity for this unheated, Mach 1.8 jet, presented in Ref. 26, used a ray-tracing technique to estimate the apparent source location as a function of frequency. The dominant source region, obtained when intensity vectors within 3 dB of the maximum vector were traced back to the jet centerline, covered $9D_j < z < 15D_j$ for St = 0.1, $8D_j < z < 13D_j$ for St = 0.2, $5D_j < z < 8D_j$ for St = 0.4, and $2D_j < z < 4D_j$ for St = 0.8, consistent with the idea that the source of large-scale turbulent mixing noise contracts and moves upstream as frequency increases. In the far field ($40D_j$ arc in this experiment), the frequency dependence of the location of the extended source does not translate into a large change in angle such that it is possible to define angles relative to a single MARP (measurement array reference point). In the near-field, however, the assumption of a frequency-independent MARP is troublesome as the changes in the apparent maximum source region greatly influences the appropriate definition of the directivity angles.

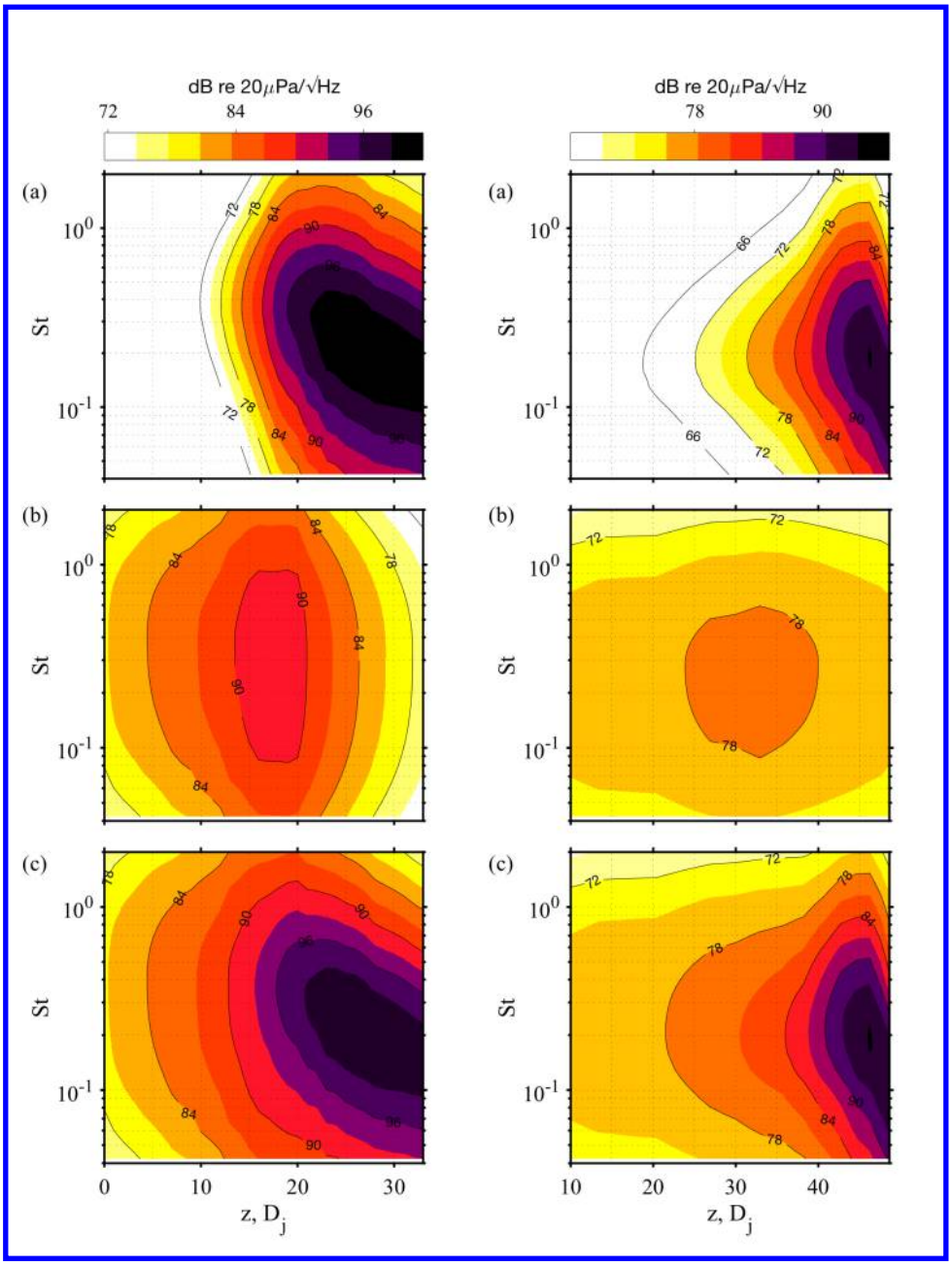

Figure 9 Predicted autospectral density levels on the $10D_j$ line array (left) and the $40D_j$ arc (right) using the (a) LSS and (b) FSS-educed wavenumber spectra from the same location and (c) the combined prediction, L_{far} from Eq. (11), as a function of downstream distance, z, scaled by jet diameter, D_j.

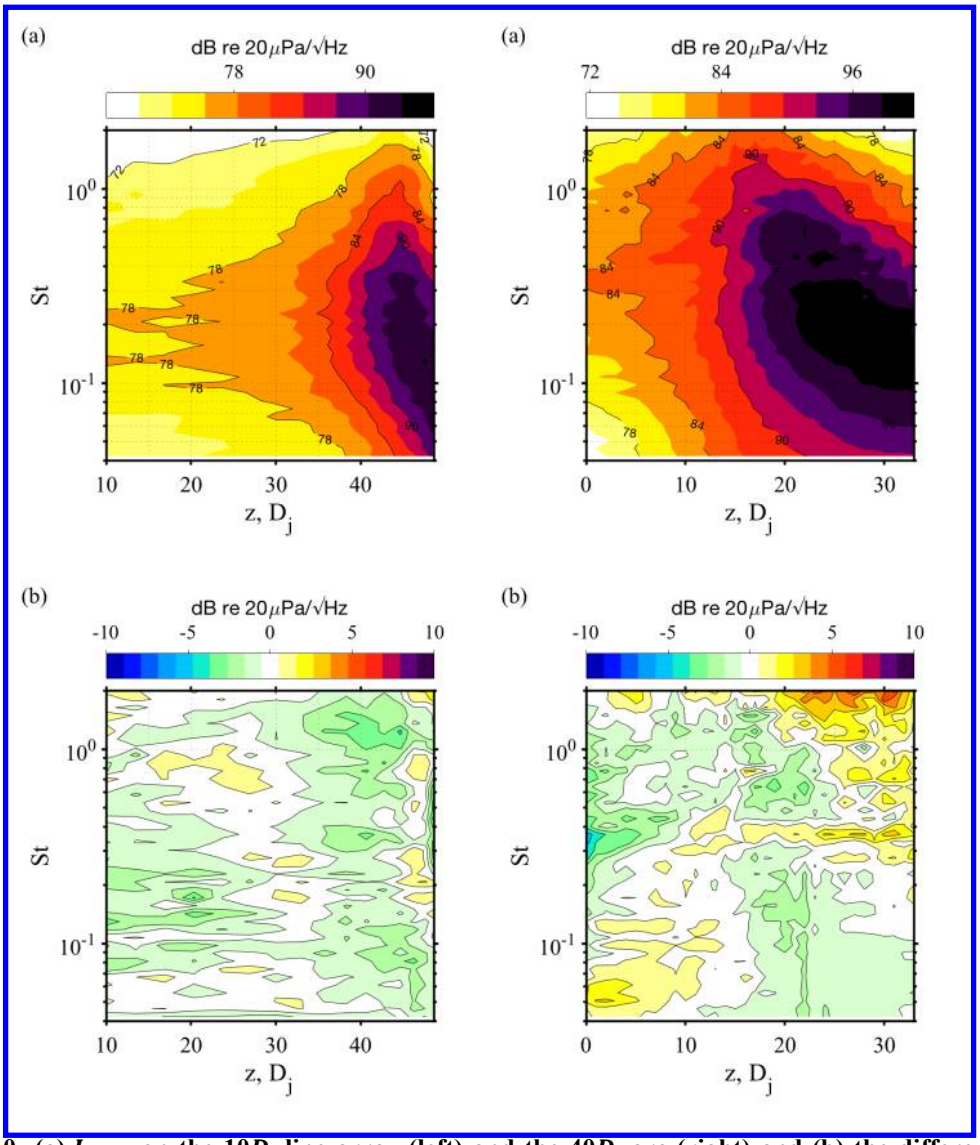

Figure 10 (a) $L_{\mathbf{meas}}$ on the $10D_j$ line array (left) and the $40D_j$ arc (right) and (b) the difference between $L_{\mathbf{far}}$ (Figure 9(c) from the same location) and $L_{\mathbf{meas}}$.

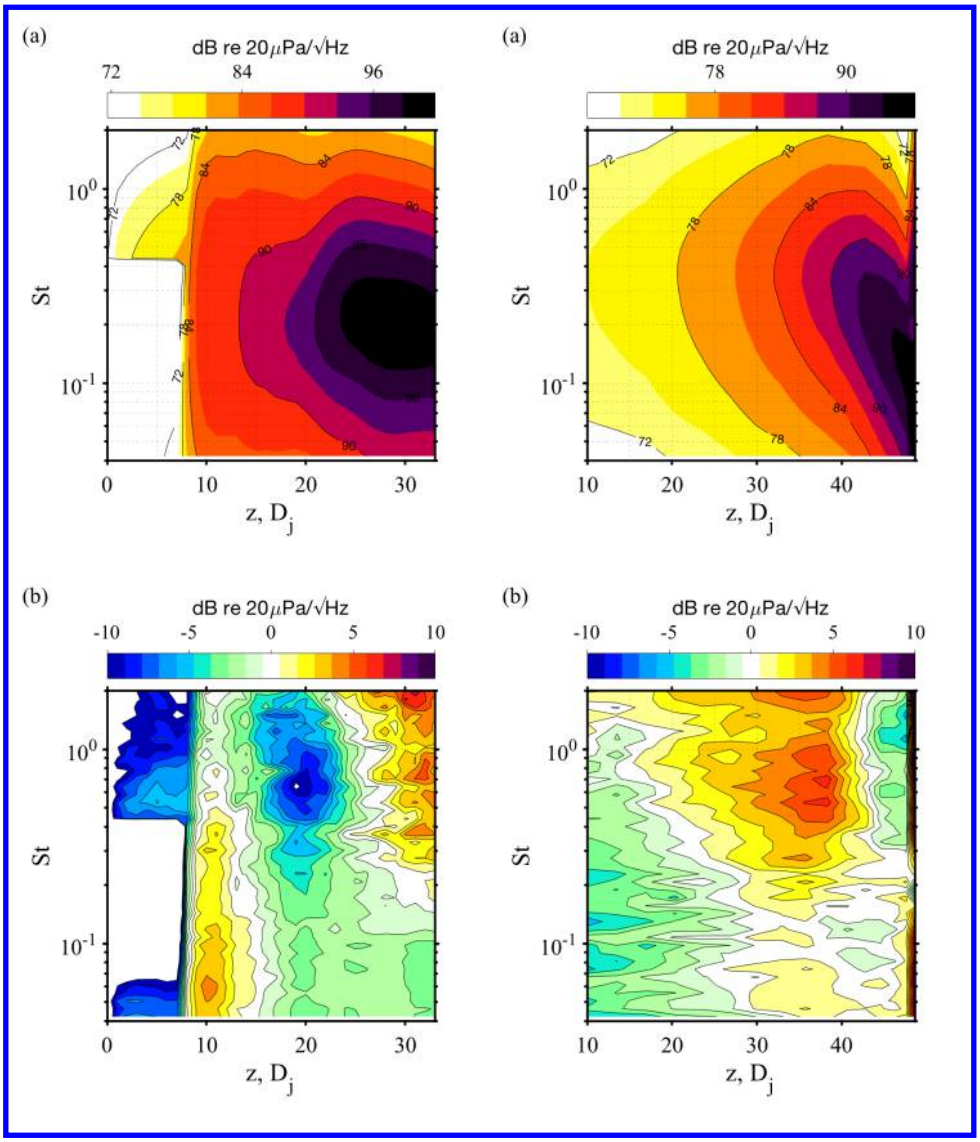

Figure 11 (a) L_{far} predicted on the $10D_j$ line array using $|G_0|$ from the $40D_j$ arc (left) and L_{far} predicted on the $40D_j$ arc using $|G_0|$ from the $10D_j$ line array (right) and (b) the difference between L_{far} in (a) and L_{meas} (shown in Figure 10(a)).

Conclusions

Autospectral densities from an unheated Mach 1.8 jet have been employed in a two-step process to obtain a wavepacket representation of the large-scale turbulent mixing noise that functions as an equivalent source model. The process begins with a similarity spectra decomposition to obtain the spatial distribution of LSS autospectral densities, which are used to obtain frequency-dependent, data-educed axial wavenumber spectra each associated with an equivalent source wavepacket. The wavenumber spectra obtained at both a $10D_j$ line array and a $40D_j$ arc exhibit two regimes of self-similarity with a transition band in between. For this unheated Mach 1.8 jet, the lower St self-similar regime corresponds to convectively subsonic case. The wavenumber spectra can be used to predict the directional portion of the sound field associated with the turbulent mixing noise.

Field predictions from the single wavepacket model do not account for noise outside the dominant radiation lobe. Addition of an uncorrelated source distribution derived from the similarity spectra decomposition associated with the fine-scale turbulent mixing noise creates a model that can predict the rest of the field. The ability of the wavepacket-plus-uncorrelated-distribution to predict field levels has been tested using measurements on a $10D_j$ line

array and a $40D_j$ arc. When predicting the field at the input location, the model's average error is less than 2 dB for St = 0.04-1.8 for the near-field array and St=0.04-3.5 for the far-field arc. When predicting the field at the other location, the model's average error is less than 2 dB for St = 0.04-0.25 but increases for larger St because the apparent directivity changes from near to far field. Likely this is because the extended nature of the source makes complicates the definition of angles in the near field. A frequency-independent definition of angles is suitable for far-field decompositions, but the frequency-dependent source extent and location need to be accounted for when the data-educed wavenumber spectra are obtained from or used to predict near-field levels.

Acknowledgments

The measurements were supported under a travel invitation fellowship by the Japan Society for the Promotion of Science. Analysis was supported in part through a grant from the Office of Naval Research Grant N000141410494 for developing wavepacket-based models for jet noise from tactical aircraft.

References

[1] Tam, C. K. W., and Burton, D. E., "Sound generated by instability waves of supersonic flows. Part 1. Two-dimensional mixing layers," *Journal of Fluid Mechanics*, Vol. 138, 1984, pp. 249-271.

[2] Tam, C. K. W., and Burton, D. E., "Sound Generation by the Instability Waves of Supersonic Flows. Part 2. Axisymmetric Jets," *Journal of Fluid Mechanics*, Vol. 138, 1984, pp. 273-295.

[3] Jordan, P., and Colonius, T., "Wave packets and turbulent jet noise," *Annual Review of Fluid Mechanics*, Vol. 45, 2013 pp. 173-195.

[4] Tam, C. K. W., Viswanathan, K, Ahuja, K. K., and Panda, J. "The Sources of Jet Noise: Experimental Evidence," *Journal of Fluid Mechanics*, Vol. 615, 2008, pp. 253-292.

[5] Viswanathan, K., "Aeroacoustics of hot jets," *Journal of Fluid Mechanics*, Vol. 516, 2004, pp. 39-82.

[6] Reba, R., Narayanan, S., and Colonius, T., "Wave-packet models for large-scale mixing noise," *International Journal of Aeroacoustics*, Vol. 9, 2010, pp. 533-558.

[7] Reba, J., Simonich, J., and Schlinker, R., "Sound Radiated by Large-Scale Wave-Packets in Subsonic and Supersonic Jets," AIAA Paper 2009-3256, May 2009.

[8] Koenig M, Cavalieri, A. V. G., Jordan, P., Delville, J., Gervais Y., and Papamoschou, D., "Farfield filtering and source imaging of subsonic jet noise," *Journal of Sound and Vibration*, Vol. 332, No. 18, 2013, pp. 4067–4088.

[9] Morris, P. J., "A note on noise generation by large scale turbulent structures in subsonic and supersonic jets," *International Journal of Aeroacoustics*, Vol. 8, No. 4, 2009, pp. 301–315.

[10] Papamoschou, D., "Wavepacket Modeling of Jet Noise Sources," AIAA Paper 2011-2835, 2011.

[11] Papamoschou, D., "Prediction of Jet Noise Shielding," AIAA Paper 2010-0653, 2010.

[12] Neilsen, T. B., Gee, K. L., Harker, B. M., and James, M. M., "Level-educed Wavepacket Representation of Noise Radiation from a High-Performance Military Aircraft", AIAA SciTech, January 2016, AIAA 2016-1880.

[13] Tam, C. K. W. and Chen, K. C., "A statistical model of turbulence in two dimensional shear layers," *Journal of Fluid Mechanics*, Vol. 92, 1979, pp. 303-326 .

[14] Tam, C. K. W., "Stochastic model theory of broadband shock associated noise from supersonic jets," *Journal of Sound and Vibration*, Vol. 116, 1987, pp. 265-302.

[15] Tam, C. K. W., Golebiowsky, M. and Seiner, J. M., "On the Two Components of Turbulent Mixing Noise from Supersonic Jets," AIAA Paper 96-1716, 1996.

[16] Tam, C. K. W. and Zaman, K., "Subsonic Noise from Nonaxisymmetric and Tabbed Nozzles," *AIAA Journal*, Vol. 38, 2000, pp. 592–599.

[17] Tam, C. K. W., Pasouchenko, N. N., and Schlinker, R. H., "Noise source distribution in supersonic jets," *Journal of Sound and Vibration*, Vol. 291, 2006, pp. 192-201.

[18] Viswanathan,K., "Analysis of the two similarity components of turbulent mixing noise," *AIAA Journal*, Vol. 40, 2002, pp. 1735–1744.

[19] Viswanathan, K., "Does a Model-Scale Nozzle Emit the Same Jet Noise as a Jet Engine?" *AIAA Journal*, Vol. 46, 2008, pp. 1715-1737.

[20] Viswanathan, K., and M. J. Czech, "Role of jet temperature in correlating jet noise," *AIAA Journal*, Vol. 47, 2009, pp. 1090-1106.

[21] Schlinker, R. H., Liljenberg, S. A., Polak, D. R., Post, K. A., Chipman, C. T., and Stern, A. M., "Supersonic Jet Noise Source Characteristics & Propagation: Engine and Model Scale," AIAA Paper 2007-3623, May 2007.

[22] Neilsen, T. B., Gee, K. L., Wall, A. T., and James, M. M., "Similarity spectra analysis of high-performance jet aircraft noise," *Journal of the Acoustical Society of America*, Vol. 133, No. 4, 2013, pp. 2116-25.

[23] Neilsen, T. B., Gee, K. L., Wall, A. T., James, M. M., and Atchley, A. A., "Comparison of supersonic full-scale and laboratory-scale jet data and the similarity spectra for turbulent mixing noise," *Proceedings of Meetings on. Acoustics,* Vol. 19, 2013, paper 040071.

[24] Greska, B., "Supersonic jet noise and its reduction using microjet injection," Ph.D. thesis, The Florida State University, FAMU-FSU Collage of Engineering, 2005.

[25] Akamine, A., Nakanishi, Y., Okamoto, K., Teramoto, S., Okunuki, T., and Tsutsumi, S., "Acoustic phenomena from correctly expanded supersonic jet impinging on inclined plate," AIAA J. 53, 2061-2067 (2015).

[26] Gee, K. L., Akamine, M., Okamoto, K., Neilsen, T. B., Cook, M. R., Teramoto, S., Okunuki, T., "Characterization of Supersonic Laboratory-Scale Jet Noise with Vector Acoustic Intensity," submitted to AIAA Aviation 2017**.**

[27] C. K. W. Tam, K. Viswanathan, K. K. Ahuja, and J. Panda, "The sources of jet noise: experimental evidence", J. Fluid Mech. **615**, 253-292 (2008).

[28] Viswanathan, K., "Investigation of noise source mechanisms in subsonic jets", AIAA J. **46**, 336-355 (2008).

[29] Vaugh, A. B., Neilsen, T. B., Gee, K. L., Okamoto, K., and Akamine, M., "Spatial variation in similarity spectra decomposition of a Mach 1.8 laboratory-scale jet, Accepted to Proc. Mtgs. Acoust. 2017.